FEM MODELING AND EXPERIMENTAL VALIDATION OF QUENCH-INDUCED DISTORTIONS OF LARGE SIZE STEEL FORGINGS

Y. Bouissa, N. Bohlooli, D. Shahriari, H. Champliaud, J-B. Morin, M. Jahazi

Article published in the " Journal of Manufacturing Processes", Volume 58, October 2020, Pages 592-605

The final publication is available at https://doi.org/10.1016/j.jmapro.2020.08.042

FEM modeling and experimental validation of quench-induced distortions of large size steel forgings

Y. Bouissa[1*], N. Bohlooli[1], D. Shahriari[1], H. Champliaud[1], J-B. Morin[2], M. Jahazi[1*]

[1] *Department of Mechanical Engineering, École de technologie supérieure, 1100 Notre-Dame Street West, Montreal, QC, Canada H3C 1K3*

[2] *Finkl Steel Inc., 100 McCarthy, Saint-Joseph-de-Sorel, QC , Canada, J3R 3M8*

[*] *Corresponding Authors: e-mail: yassine.bouissa@gmail.com / Mohammad.jahazi@etsmtl.ca*

Abstract

Industrial-level water quenching operations generally lead to high residual stresses and distortion, especially for large steel parts, due to the high temperature gradient present. In this work, a 3D Finite Element (FE) model was used to simulate the water quenching process of a large size forged block made of high-strength steel in a bid to predict the induced distortion and residual stresses. The FE model considers the coupling between the thermal, mechanical and metallurgical fields and in addition to that the mechanical properties related to each phase at different temperatures were experimentally generated to feed the FE model with reliable material data. Furthermore, an experimental approach was designed to accurately measure the shape change after quenching. The results indicated that the FE model was able to predict the pattern of the distortion induced by the quench process. Also, the value of the maximum magnitude of thickness reduction was predicted at the center region of the block with a deviation of 0.5 mm.

Keywords: Prediction of distortion, FEM, residual stress, quenches modeling, large forging, distortion measurement.

1. Introduction

Quenching and tempering are two mandatory and inevitable steps in the manufacturing cycle of a very large family of forged steel parts (landing gears, large shaft, mold steels, etc.). The purpose of the quench process is to produce, through a phase transformation process, hard phases (martensite and/or bainite) that significantly improve the mechanical properties of the material [1, 2]. Nevertheless, the large size of the steel components imposes considerable thermal inertia during quenching (Biot numbers in excess of 20), resulting in significant temperature gaps between the surface and the core of the component. This inhomogeneity in temperature distribution also triggers uncontrolled residual stresses that could result in distortions in most cases, and even cracks, which could potentially lead to part scrapping [3]. In order to anticipate and reduce the distortion effects after quenching, conventional practices such as designing symmetrical parts or over-dimensioning are often used. However, in the case of complex geometries (gears, landing gears, etc.) [4], these techniques may not always represent practical solutions when it comes to ensuring components' functionalities, or maintaining an adequate product processing cost as a direct consequence of material removal overestimation (extra thickness of the initial material which must be removed at the end of the quench process), which brings additional costs [5].

Distortion during steel hardening is a nonlinear phenomenon that involves several fields with strong couplings and complex interactions between each of them [6, 7]. As a result, the characteristics and patterns of quench-induced distortion are hard to predict. On the other hand, the non-linear interactions between the involved variables, limit the use of analytical methods for modeling and predicting deformation extent and severity. However, the reliability of distortion predictions depends wholly on accurate quantification of the interactions between temperature and phase transformation since they directly affect the end shape of the part. The latter can only be precisely achieved with a comprehensive understanding of the conjugate consideration of thermal, mechanical, and metallurgical interactions and their relative sequences during the quench process. For example, in the presence of a large range of cooling rates [8] (due to part size, shape,

quench intensity, hardenability, etc.) different scenarios of phase transformation are expected in the same component (i.e., time history of phase transformations).Therefore, quantifying phase transformation during the quench process is of critical importance because of its impact on distortion characteristics. The strain state during hardening is directly correlated with distortion, and is mainly driven by the thermal expansion and the volume change of the newly formed microstructures as a result of phase transformation [8]. The strain state is also affected by the transformation-induced plasticity (TRIP) phenomenon, which causes a permanent deformation of the soft austenite phase (parent phase) [9]. The TRIP strain effect is related to the coexisting mismatch in density between the parent austenite and the newborn harder phase (martensite or bainite) [10] even if the yield stress is not reached [11]. However, experimental determination of the phase transformation plasticity parameter, *K*, remains difficult, especially if it is considered as a temperature-dependent function. The final overall distortion of the quench part is obtained by a superposition of the above effects [3, 12].

In recent years, with the advent of high performance computing capabilities, numerical approaches such as Finite Element Modeling (FEM) have been used to analyze different aspects of the quenching process, and some algorithms have been implemented in commercial software [13]. Nonetheless, given the complexity of this process, as well as a lack of accurate material data (e.g., phase mechanical properties), simplifications have been applied. These simplifications include the non-consideration of the TRIP effect [14, 15] , using a 2D analysis approach, or focusing only on the heat transfer aspect [16, 17]. Furthermore, most of the investigations reported in the literature are devoted to laboratory size specimens [7, 18-20]. Predictions made using the above simplifications and small size samples could not accurately anticipate the quench-induced distortion of industrial size components. For example, the size and the shape of the part asymmetrically affect the heat transfer within the part, the phase transformation at different locations, and hence, the distribution of the residual stresses and properties. This can only be circumvented if a 3D

modeling approach is used [4, 13] and accurate material data (e.g., properties of each phase) are employed [21].

Furthermore, validating simulations at industrial scale requires significant human and material resources to carry out experimental measurements. In addition, it is generally very difficult to determine error sources [13]. Multiscale validation methods have been used to extrapolate the validation of simulations to different scales when the phenomena at stake are supposed to be separable and scale-independent. However, this strategy is no longer applicable for the quench process, due to the fact that the fields involved are strongly coupled, and their evolution is size-dependent [13]. Therefore, a direct and reliable method of measurement at the industrial scale is needed. Finally, it must be noted that little information is available in the literature on the experimental validation of shape change after quenching of large steel components [12]. This limitation is mainly due to the difficulty of accurately tracking the distortion when surfaces are damaged or roughened by oxidation. Thus, several studies that used the FEM to predict the distortion did not present any experimental validations [5, 14, 19, 22, 23].

The present paper encompasses a comprehensive methodology for 3D FEM modeling of large size steel forgings during the quenching process, validated by experimental measurement of the quench-induced distortions. Considering the limited availability of thermomechanical material data for this family of steels (mold steels) and particularly the investigated one which is extensively used in the forge industry, the majority of the needed properties for FEM modeling was produced experimentally using the Gleeble^{TM} 3800 thermo-mechanical simulator and a high-resolution dilatometer (DIL-805A/D) in order to reduce as much as possible the impact of material uncertainties on simulations. The approach proposed to measure distortions after quenching is detailed, as very little is also available in the measurement of quenched induced distortion in large size components. Providing such data could be an asset to a large number of researchers and industrials.

2. Simulation of Quenching

Figure 1 shows the main fields of the modeling and their mutual interactions that need to be considered for a comprehensive simulation of the quench process [24]:

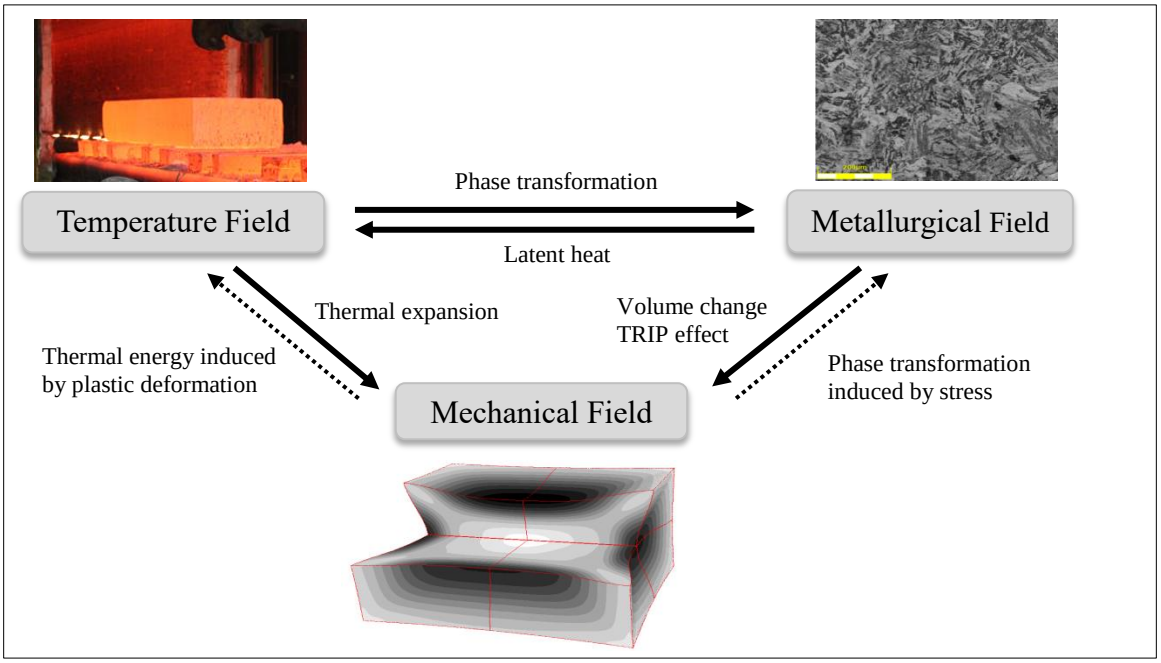

Figure 1: Description of the existing interactions between the involved fields during quench modeling

In the following section, a summary of the mathematical formulation that describes the evolution of each field, and constitutes the basis for the simulation, is provided.

Considering the fact that the plastic deformations created during the quench are limited (2 to 3%), the thermal energy generation induced by plastic deformation was neglected [25]. Furthermore, the effect of stress that triggers phase transformation was not considered in the present investigation.

2.1. Temperature field

The heat transfer during quenching was modeled using the heat equation:

$$\rho C_p \frac{\partial T}{\partial t} = \lambda \left(\frac{\partial^2 T}{\partial x^2} + \frac{\partial^2 T}{\partial x^2} + \frac{\partial^2 T}{\partial x^2} \right) + \dot{q} \qquad (1)$$

where ρ , C_p, λ and $\dot{q}$ are density, heat capacity, thermal conductivity and the internal thermal energy released due to phase transformation, respectively.

The internal thermal energy $\dot{q}$ could be expressed as a function of the latent heat, ΔH_k, and the volume phase fraction, ξ_k, as follows:

$$\dot{q} = \sum \Delta H_k \, . \, \frac{d\xi_k}{dt} \tag{2}$$

Under this condition, the heat transfer coefficient becomes [26]:

$$-\lambda \frac{\partial T}{\partial n} = h(T_s - T_a) = (h_{convection} + h_{radiation})(T_s - T_a) \tag{3}$$

The heat transfer due to radiation could be expressed as follows:

$$h_{radiation} = \sigma . \epsilon . \left({T_s}^2 + {T_a}^2\right)(T_s + T_a) \tag{4}$$

where σ, ϵ, T_s and T_a are Stefan-Boltzmann constant, emissivity coefficient, surface temperature and ambient temperature, respectively. It must be noted that the heat transfer coefficient during water quenching is considered as the most significant parameter for the calculation of the thermal field due to the fact that it varies as a function of temperature [18]. In the present work, the heat transfer coefficient during water quenching, as illustrated in Figure 2, was adapted from a previous publication by the current authors due to the similarity between the steel grades and forging block thickness [27], while the one used for air cooling was extracted from the work of Dung-An Wang (2013) [28]. Finally, in agreement with the literature, the emissivity coefficient value, ϵ, was considered to be 0.6 during air cooling [29].

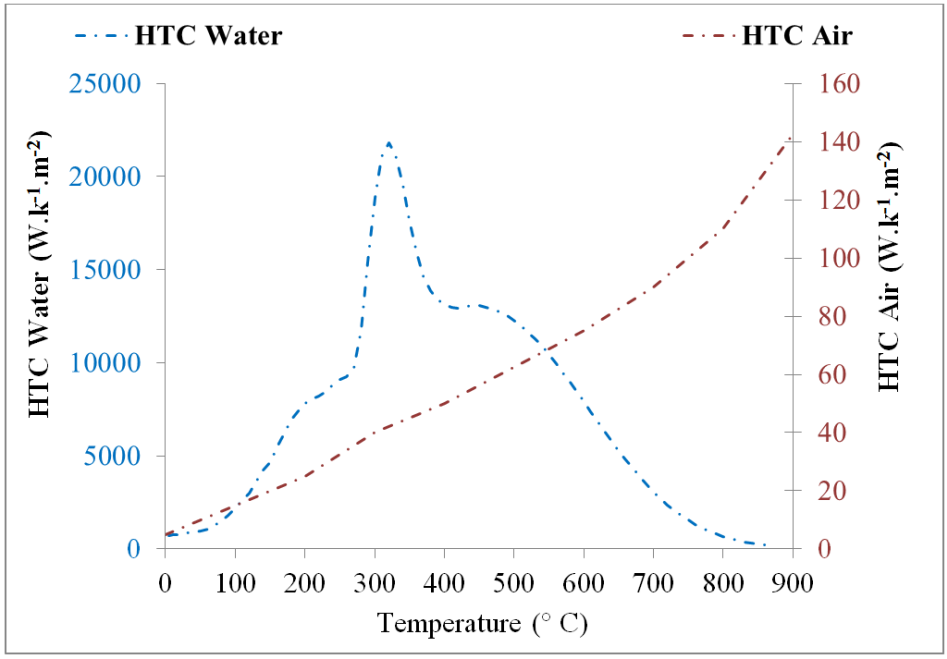

Figure 2: Heat transfer coefficient during water quenching [27] and air cooling [28]

2.2. Metallurgical field

During the quenching process, the evolution of the volume fraction of transformed phases during continuous cooling could be obtained from the Johnson-Mehl-Avrami-Kolmogorov (JMAK) for diffusion controlled transformations (e.g., ferrite- perlite) [27, 30, 31]. For a given temperature T_i at time t_i , JMAK equation could be written as follows:

$$\xi_i = 1 - exp(-bt_i{}^n) \tag{5}$$

where *b* and *n* represent the constants of the JMAK model.

Any considered cooling temperature curve could be subdivided to several elementary isothermal states (T_i, t_i). The incubation time in the is considered satisfied when the unity is reached by Scheil's sum, S, as follows:

$$S = \sum_{i=1}^{n} \frac{\Delta t_i}{\tau_i} = 1 \tag{6}$$

Where Δt_i , τ_i represents, the time step and the incubation time at time t_i , respectively.

The phase volume fraction for the fictitious time t_i^* could be written as follows:

$$\xi_i^* = 1 - exp\{-b_{i+1}(t_i^*)^{n_{i+1}}\} \quad (7)$$

Where the fictitious time could be calculated by the following equation:

$$t_i^* = \left(\frac{-\ln(1-\xi_i)}{b_{i+1}}\right)^{\frac{1}{n_{i+1}}} \quad (8)$$

And finally, the transformed volume phase fraction at time t_{i+1} , be calculated using equation (9):

$$\xi_{i+1} = \left(\xi_i^{\gamma} + \xi_i\right)\xi_{max}\ \xi_i^* \quad (9)$$

For the time step t_i, ξ_i^{γ} represent the volume phase fraction of austenite and ξ_{max} the maximum volume phase fraction that could be transformed.

In case where the phase transformation is displacive (martensite), the Koistinen-Marburger model [31] could describe the volume phase fraction evolution, as follows:

$$\xi_m = 1 - exp(-\alpha(M_s - T)) \quad (10)$$

Where α represent the constant of Marburger, and M_s , the martensite start temperature.

It should be noted that in the present work, a linear phase mixture rule, as described in equation (11), was used to obtain macro-level material properties [19, 32].

$$P = \sum P_k \xi_k \quad (11)$$

In the above equation, P represents the material property at the macro level, and P_k, that of each micro-constituent.

2.3. Mechanical field

2.3.1. Strain model

The shape changes during steel hardening are directly linked to the history of generated strains [12]. The volume change could be correlated to the spherical strain tensor, while the distortion could be correlated to the deviatoric part [33]. The total strain induced in the material as a result of quenching could be represented by the sum of five strain components:

$$d\{\varepsilon\} = d\{\varepsilon_e\} + d\{\varepsilon_{th}\} + d\{\varepsilon_{tp}\} + d\{\varepsilon_{tr}\} + d\{\varepsilon_p\} \quad (12)$$

where $d\{\varepsilon\}, d\{\varepsilon_e\}, d\{\varepsilon_{th}\}, d\{\varepsilon_{tp}\}, d\{\varepsilon_{tr}\}$ and $d\{\varepsilon_p\}$ represent the total, elastic, thermal, phase transformational, and transformation plasticity, and plastic increments of deformation, respectively. Equations (13-(15) describe the formulation of the thermal [34], phase transformation [35] and plastic strain increment, as reported in [30].

Thermal strain increment

$$d\{\varepsilon_{th}\} = \sum_{k=1}^{p} \xi_k \alpha_k dT \quad (13)$$

Where α_k is the thermal expansion coefficient of the phase k.

Phase transformation strain increment

$$d\{\varepsilon_{tp}\} = \sum_{k=1}^{p-1} \frac{1}{3} \Delta_k d\xi_k \quad (14)$$

Where Δ_k is the structural dilation due to phase transformation

Plastic strain increment

$$d\{\varepsilon_p\} = d\lambda \frac{\partial f}{\partial\{\sigma\}} \quad (15)$$

$$f = \sqrt{\frac{3}{2}\{S\}\{S\}^T} - \sigma_Y = \bar{\sigma} - \sigma_Y = 0 \quad (16)$$

In the above equations, f represents the potential plastic function in the stress space, $d\lambda$ is the constant plastic multiplier, σ_Y the yield stress, and $\bar{\sigma}$ is the equivalent stress.

Transformation-Induced Plasticity (TRIP)

The mathematical form of the strain rate due to TRIP could be expressed as follow [36] using Desalos model:

$$d\{\varepsilon_{tr}\} = \frac{3}{2} K_k \{S\} 2\left(1 - \xi_k\right) d\xi_k \quad (17)$$

where K_k is a constant due to the transformation-induced plasticity (TRIP) and $\{S\}$ the stress tensor deviator.

Plastic Memory Loss Due To Phase Transformations

It must be noted that the new formed phases do not necessarily inherit the strain hardening history (memory of deformation) experienced by the initial phase (austenite) [10]. Depending on whether the new phase undergoes a full (γ_k =1) or partial ($0 < \gamma_k <1$) strain hardening recovery, the inherited average strain at time $t + \Delta t$ could be described as follows [31] :

$$\bar{\varepsilon_k}(t+\Delta t) = (1-\gamma_k)\frac{\xi_k(t)\bar{\varepsilon_k}(t) + \left(\xi_k(t) + \Delta\xi_k\right)\Delta\bar{\varepsilon}}{\xi_k(t) + \Delta\xi_k} + \gamma_k\bar{\varepsilon}(t+\Delta t) \tag{18}$$

where $\gamma_k$is the memory coefficient of the phase k.

2.3.2. Stress model

The inverse generalized Hook's law for elastic behavior could be expressed as follows:

$$\{\varepsilon_e\} = [D_e^{-1}(T)]\{\sigma\} \tag{19}$$

Derivation of equation (19), results in:

$$d\{\varepsilon_e\} = \frac{\partial[D_e^{-1}(T)]}{\partial T}dT\{\sigma\} + [D_e^{-1}(T)]d\{\sigma\} \tag{20}$$

Multiplying equation (20) by the elastic matrix $[D_e(T)]$, leads to:

$$[D_e(T)]d\{\varepsilon_e\} = [D_e(T)]\frac{\partial[D_e^{-1}(T)]}{\partial T}dT\{\sigma\} + [D_e(T)][D_e^{-1}(T)]d\{\sigma\} \tag{21}$$

with:

$$d\{\sigma\} = [D_e(T)](d\{\varepsilon_e\} - \frac{\partial[D_e^{-1}(T)]}{\partial T}\{\sigma\}dT) = [D_e(T)](d\{\varepsilon_e\} - d\{\varepsilon_0\}) \tag{22}$$

and

$$d\{\varepsilon_0\} = \frac{\partial[D_e^{-1}(T)]}{\partial T}\{\sigma\}dT \tag{23}$$

$d\bar{\varepsilon_p}$ represent the increment of the equivalent plastic strain

$$d\{\varepsilon_p\} = d\bar{\varepsilon_p}\frac{\partial\bar{\sigma}}{\partial\{\sigma\}} = d\lambda\frac{\partial f}{\partial\{\sigma\}} \tag{24}$$

Considering that $\sigma_Y\left(\int d\bar{\varepsilon_p}, T\right)$, the total differential form of the equation (16) could be written as:

$$\left(\frac{\partial \bar{\sigma}}{\partial\{\sigma\}}\right)^T d\{\sigma\} \quad = \frac{\partial \sigma_Y}{\partial \bar{\varepsilon_p}}\, d\bar{\varepsilon_p} + \frac{\partial \sigma_Y}{\partial T} dT \tag{25}$$

$$d\bar{\varepsilon_p} = \frac{\left(\frac{\partial \bar{\sigma}}{\partial\{\sigma\}}\right)^T [D_e(T)]\left(d\{\varepsilon\} - d\{\varepsilon_{th}\} - d\{\varepsilon_{tp}\} - d\{\varepsilon_{tr}\} - d\{\varepsilon_0\}\right) - \frac{\partial \sigma_Y}{\partial T} dT}{\frac{\partial \sigma_Y}{\partial \bar{\varepsilon_p}} + \left(\frac{\partial \bar{\sigma}}{\partial\{\sigma\}}\right)^T [D_e(T)] \frac{\partial \bar{\sigma}}{\partial\{\sigma\}}} \tag{26}$$

Finally, the stress increment could be expressed as follows:

$$d\{\sigma\} = \begin{cases} [D_e(T)]\left(d\{\varepsilon\} - d\{\varepsilon_{th}\} - d\{\varepsilon_{tp}\} - d\{\varepsilon_{tr}\} - d\{\varepsilon_0\}\right) & , \bar{\sigma} < \sigma_Y \\ \left[D_{ep}(T)\right]\left(d\{\varepsilon\} - d\{\varepsilon_{th}\} - d\{\varepsilon_{tp}\} - d\{\varepsilon_{tr}\} - d\{\varepsilon_0\}\right) + d\{\sigma_0\} & , \bar{\sigma} = \sigma_Y \end{cases} \tag{27}$$

where the elastic-plastic matrix could be written as follows:

$$\left[D_{ep}(T)\right] \quad = \quad [D_e(T)] - \frac{[D_e(T)] \frac{\partial \bar{\sigma}}{\partial\{\sigma\}} \left(\frac{\partial \bar{\sigma}}{\partial\{\sigma\}}\right)^T [D_e(T)]}{\frac{\partial \sigma_Y}{\partial \bar{\varepsilon_p}} + \left(\frac{\partial \bar{\sigma}}{\partial\{\sigma\}}\right)^T [D_e(T)] \frac{\partial \bar{\sigma}}{\partial\{\sigma\}}} \tag{28}$$

and

$$d\{\sigma_0\} \quad = \quad \frac{[D_e(T)] \frac{\partial \bar{\sigma}}{\partial\{\sigma\}} \frac{\partial \sigma_Y}{\partial T} dT}{\frac{\partial \sigma_Y}{\partial \bar{\varepsilon_p}} + \left(\frac{\partial \bar{\sigma}}{\partial\{\sigma\}}\right)^T [D_e(T)] \frac{\partial \bar{\sigma}}{\partial\{\sigma\}}} \tag{29}$$

It should be mentioned that an elasto-plastic model was used in the current study [25]. The equations used to describe the stress model are based on the works of [34, 37, 38]. The above equations further highlight the complex couplings between the stress and strain during quenching.

3. Methodology

3.1. Experimental setup

A 645×868×1037 mm^3 steel block with the composition shown in Table 1 was machined in order to track volume changes after the quench and temper heat treatment cycle.

Table 1: Chemical composition of steel block (wt / %)

% C	% Mn	% Si	% Ni	% Cr	% Mo	% Cu
0.28 - 0.40	0.60 - 1.00	0.20 - 0.80	0.45 - 0.65	1.40 – 2.00	0.35 - 0.55	0 - 0.25

The flow chart of the heat treatment process, presented in Figure 3, was specifically designed for the experimental block.

The block was austenitized at 871 °C and quenched in water (6 °C) for around 2.5 h, followed by air cooling (20 °C) for 1.5 h. The quenched block was then tempered at 565 °C for about 48 hours to reduce the level of the residual stresses produced during quenching. While the tempering could very slightly affect the quench-induced distortions, the dimensional changes are, however, considered relatively negligible in this case, considering the large size of the block [21].

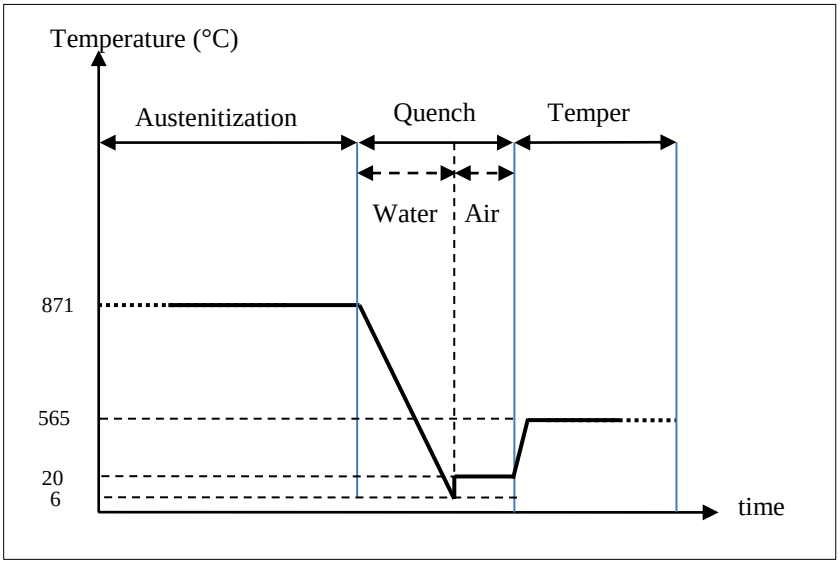

Figure 3: Heat treatment cycle

3.2. Geometrical modeling

3.2.1. 3D Surface measurement

Dimensional measurements were conducted to precisely model the surface of the block before and after heat treatment. The digitization of the 3D discrete point positions (x,y,z) was obtained using a 3D scanner (Creaform Handyscan 3D / EXAscan model - Figure 4), and based on a triangulation approach [39]. The measurement process consisted in projecting a pattern of laser lines on the object to be scanned. The reflected light coming from the object was then collected by a CCD camera for real-time data processing [39]. The triangulation process was tracked using the positional markers, which were taped onto the block in

order to create an irregular triangle mesh. In this approach, the density and positions of the markers depend principally on the size of the block and the area to be scanned; for example, edges and corners [40].

The small arms in Figure 4 (indicated ‘e’ in the figure) were added to the block to allow easier visibility during the lifting operations after austenitization.

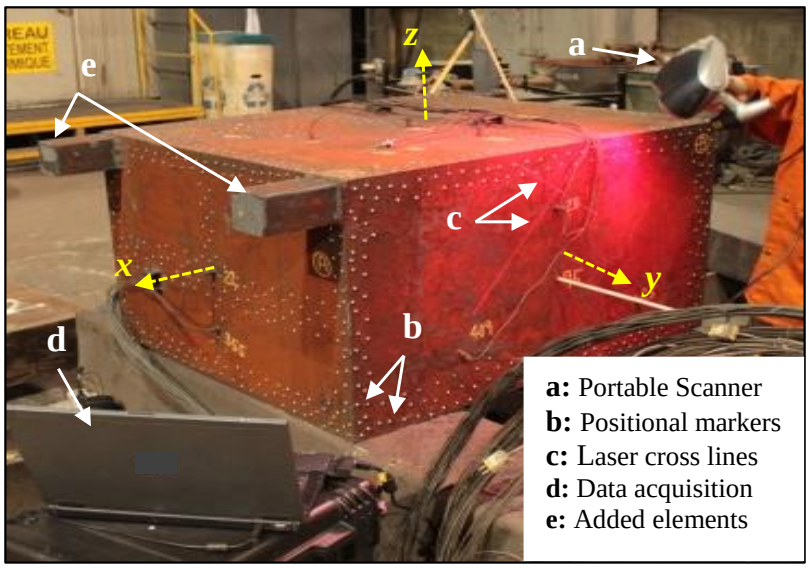

Figure 4: Measurement scanning procedure

3.2.2. 3D surface reconstruction and solid modeling

3.2.2.1. Reconstruction of 3D surfaces

The data files generated by the 3D scanners were imported in the Catia V5 DSE (Digitized Shape Editor) module to analyze and test the quality of the points distribution [39] and to remove unneeded parts such as wires, fixtures, etc. (Figure 5.a).

The main steps used to obtain the final 3D body are illustrated in Figure 5. Specifically, different functions and modules were used in Catia V to reconstruct 3D surfaces from the points cloud. The maximum deviation of the modeled surfaces within the selected points was less than 1 mm. The final reconstructed shape was obtained by assembling the six surfaces of the block (Figure 5 b). The external surface was then converted into a solid body.

The three principal axes of inertia was determined by Catia V5 for before and after quench volumes of the reconstructed block (Figure 5.b). The inertia axis system was considered as a new common reference using the following equations [41]:

$$I_{xx} = \rho \int (y^2 + z^2).dV \ , \ I_{yy} = \rho \int (x^2 + z^2).dV \ , \ I_{zz} = \rho \int (x^2 + y^2).dV \quad (30)$$

3.2.2.2. Design of the nominal cuboid used for FEM model

The shape of the part obtained before heat treatment was a non-ideal cuboid shape that was not practical to exploit as geometry input for FEM model that was developed of an ideal cuboid shape (Figure 5.b-c) before heat treatment). This 3D part was assumed to be symmetrically subjected to the same hardening effects regarding each principal axis of inertia.

The following procedure was developed to calculate the nominal dimensions (x_0, y_0, z_0) of a cuboid shape that is able to represent the responses of a real 3D block (the reverse engineered block) to temperature and distortion.

The calculation of the nominal a cuboidal block was exploiting an optimization method that minimizes an objective function f_I (residual sum of squares) (see eq. (31)) as a function of Inertia momentums ($\frac{\partial f_I}{\partial x_0} = \frac{\partial f_I}{\partial y_0} = \frac{\partial f_I}{\partial z_0} = 0$):

$$f_I = (I_{xx} - I_{xx_0})^2 + (I_{yy} - I_{yy_0})^2 + (I_{zz} - I_{zz_0})^2 \quad (31)$$

I_{xx_0}, I_{yy_0} and I_{zz_0}represent the Inertia momentum for the nominal cuboid, and they are expressed as follows:

$$I_{xx_0} = \frac{m_0 \times ({y_0}^2 + {z_0}^2)}{12}, \quad I_{yy_0} = \frac{m_0 \times ({x_0}^2 + {z_0}^2)}{12}, \quad I_{zz_0} = \frac{m_0 \times ({x_0}^2 + {y_0}^2)}{12} \quad (32)$$

where

$$m_0 = \rho . V_0 = \rho . (x_0 \times y_0 \times z_0) \quad (33)$$

Taking the calculated Inertia axis system of the 3D body after quenching as a common reference, the estimation of the relative shape change after hardening could be compared to the nominal body shape before quenching, assuming that the 3D part was symmetrically subjected to the same hardening effects regarding each principal axis of inertia.

A zoom was required at the upper surface level (z^+, Figure 5.c) of the reconstructed 3D body to illustrate the changes of the 3D surface shape along x-y plane. More specific explanation will be addressed in section 4.2.2.

Finally, the optimized 3D nominal cuboidal block (before heat treatment) was imported into the FEM software as a geometrical input. The 3D model obtained after heat treatment will be analyzed to validate FEM results in section 4.2.2.

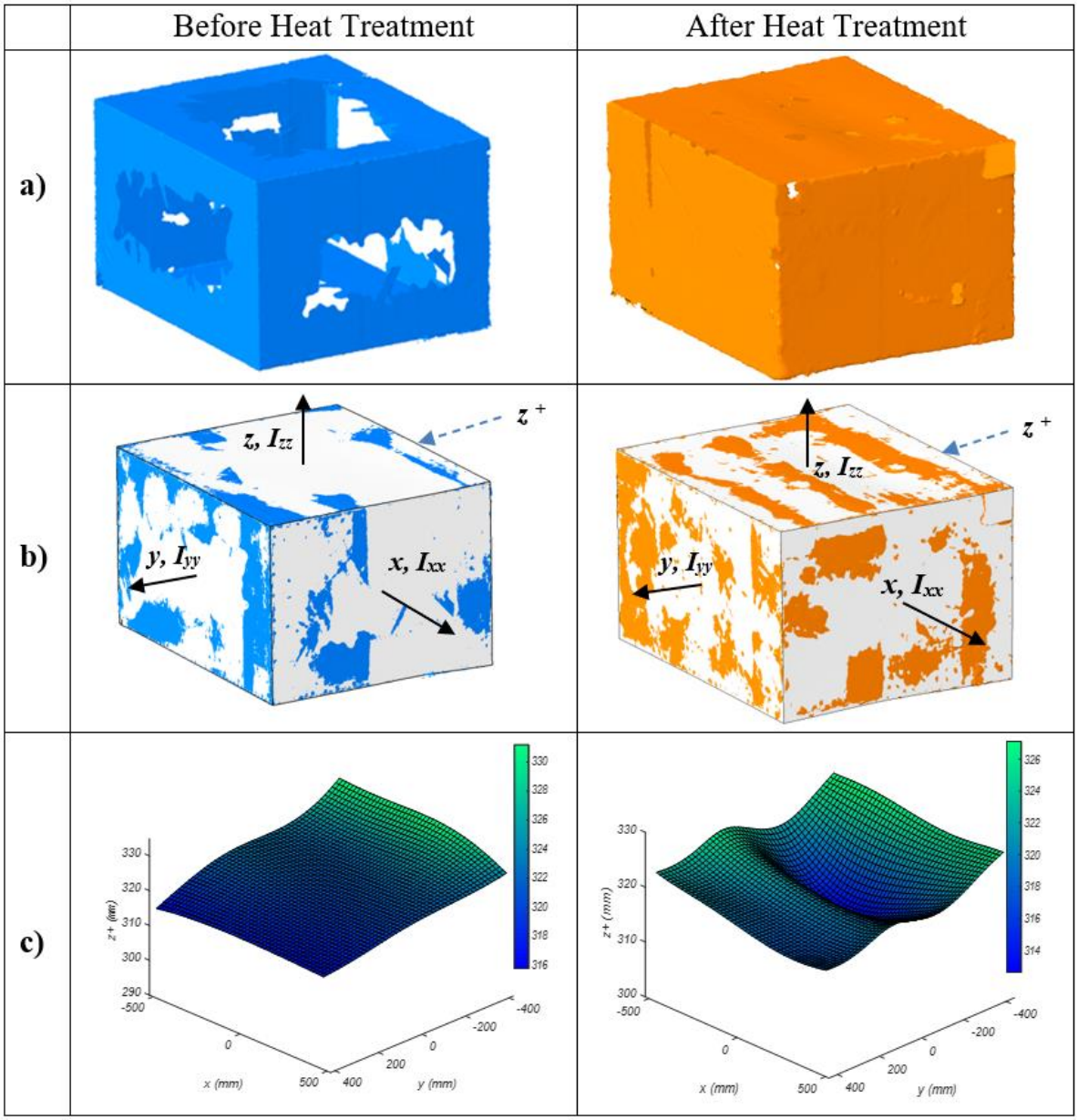

Figure 5: Procedure for shape reconstruction and body modeling using Catia V5

3.3. FEM Modeling

Forge® NxT 1.1 was used to model the part during the quench using a 3D model with three planes of symmetry. The meshing was refined by up to 898,242 tetrahedral elements (P1+/P1), which ensured grid independence. Figure 6 illustrates the dimensions of the nominal optimized solid model and the specification of the FEM model (1/8).

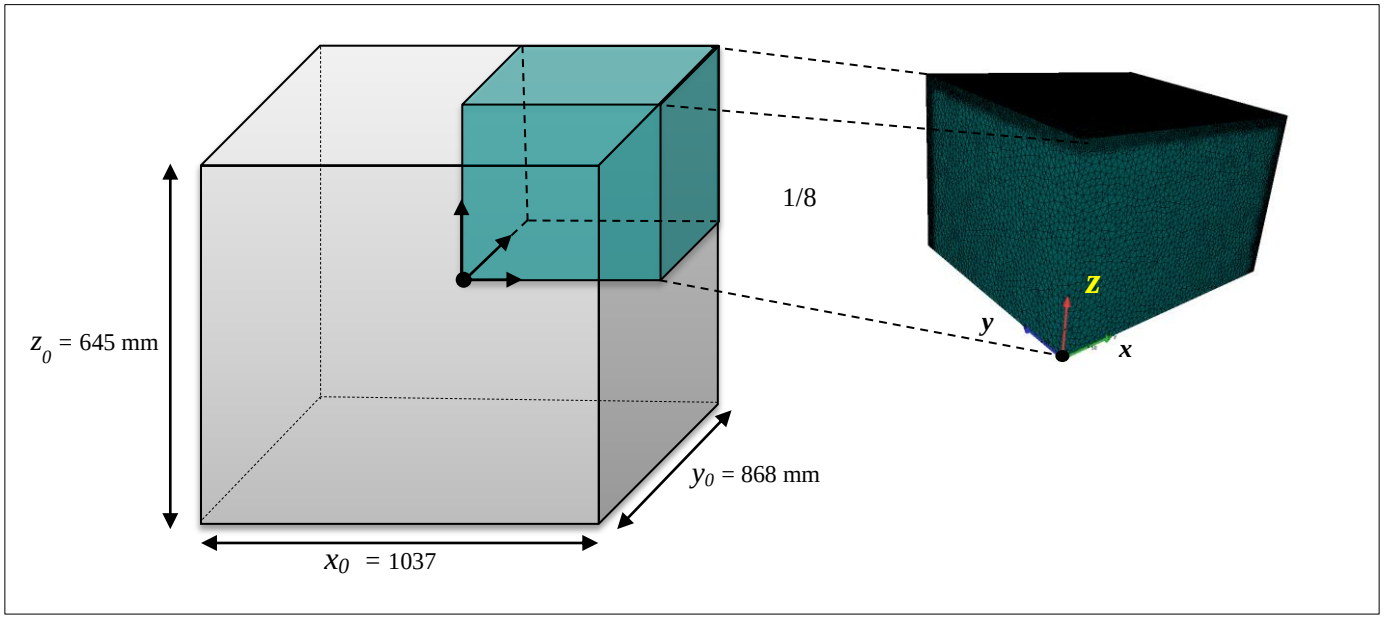

Figure 6: Dimensions of the block, and the mesh specifications

3.3.1. Material data:

3.3.1.1. Thermo-mechanical data

It is well known that the reliability of quench-induced distortion prediction in steel, where phase transformation takes place, is strongly dependent on an accurate determination of the mechanical and physical properties of each phase [13] (martensite, bainite, etc.). However, such specific data is not always available for the considered alloy, and as a result, only generic material database (e.g., JMatPro®, FEM software data base, literature, etc.) are used. In the present investigation, wherever possible, experimentally measured thermo-mechanical properties are privileged, but if unavailable, the material data generated by JMatPro® were used instead. Furthermore, a high-resolution dilatometer (DIL-805A/D) was used to obtain

the thermal expansion coefficients for each phase and the volume changes due to phase transformation, as illustrated in Figure 7 for bainitic and martensite transformations, considering that the lowest cooling rate involved in the center during water quench of the block remain still higher to form ferrite and pearlite phases.

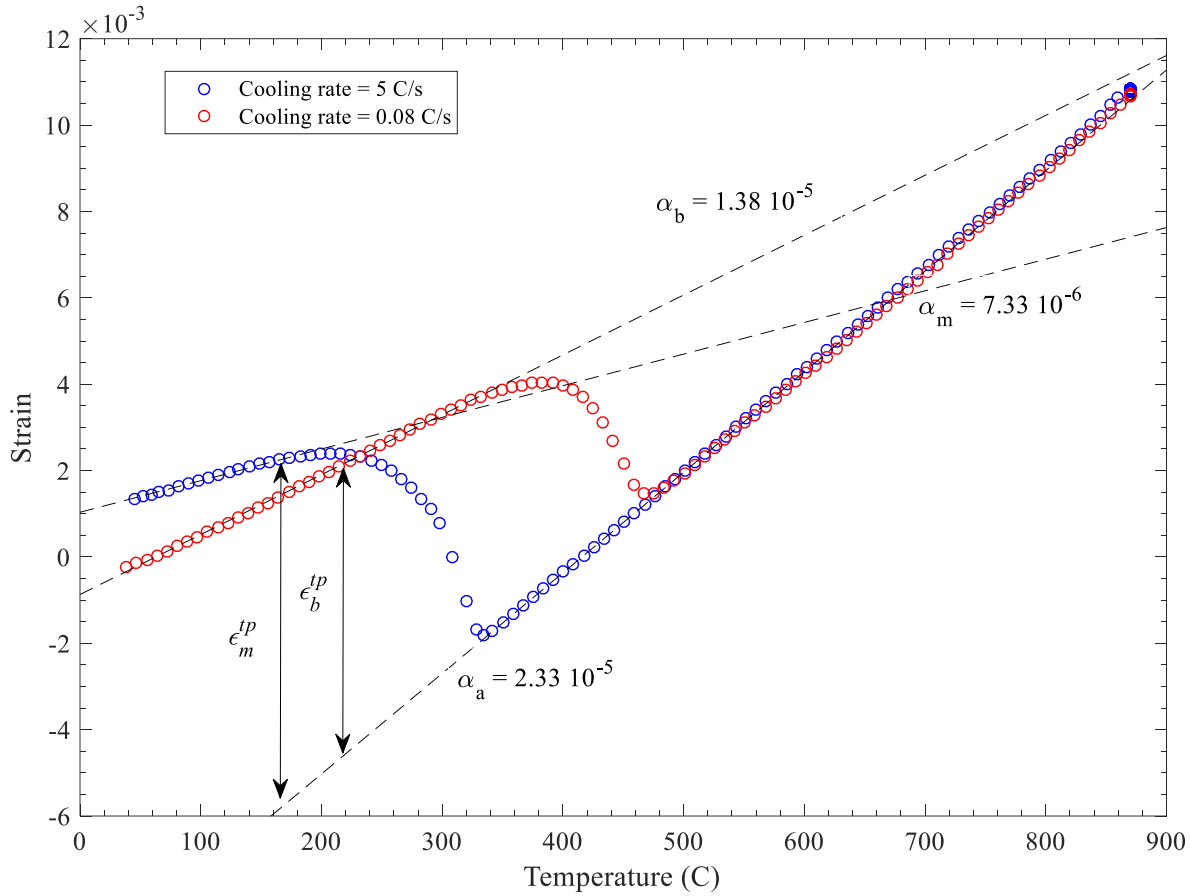

Figure 7: Extraction of thermo-mechanical coefficient using dilatometry curves

In Figure 9.c) the strain-stress curves for each phase (i.e., fully austenitic) were produced experimentally at different temperatures using the Gleeble™ 3800 thermo-mechanical simulator. The Swift law was used to model the plastic domain for each phase [42]. The calculation of the flow stress over the entire temperature range of the heat-treatment process was determined using linear interpolation and/or extrapolation. The above approach of using a combination of experimental data, Swift law, and the interpolation to other temperatures will further increase the reliability and consistency of residual stress predictions. Considering that material flow during quenching is governed by a quasi-static regime [43], the strain rate was expected to

be low. Therefore, in the present work, a strain rate of 10^{-3} s^{-1} was used for the tensile test experiments. Martensitic and bainitic single-phase samples were produced by heat treatments (quenching and austempering). The tensile samples were machined based on the ASTM E8 standard Figure 8.b). In order to increase the accuracy of the results obtained, an extensometer was installed in the gage length region of the tensile samples during all tests, as shown in Figure 8.a).

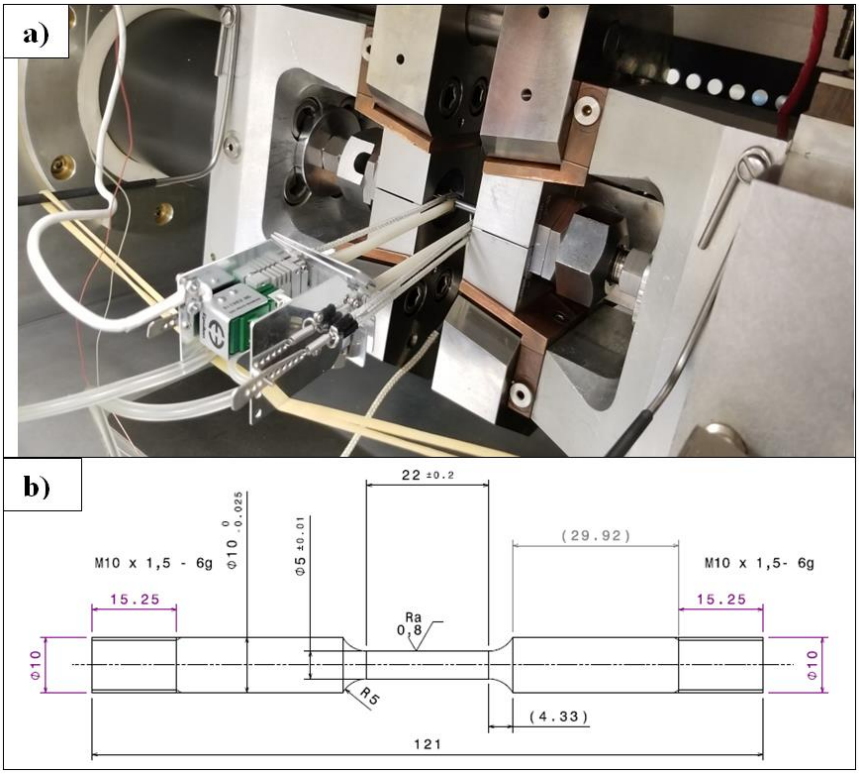

Figure 8: Material flow stress determination - a) Hot tensile testing set-up for Gleeble™ 3800 , b) Dimensions of the tensile test specimens

For each phase (austenite, bainite and martensite), the Young's modulus was calculated for selected temperatures from the tensile tests, and the following equation was used to model the evolution of the Young's modulus with temperature (Figure 9.b) [44]:

$$E(T) = E_{T_0} \exp\left\{-\frac{1}{2}\left(\frac{T-T_0}{e_3}\right)^{e_1} - \frac{1}{2}\left(\frac{T-T_0}{e_4}\right)^{e_2}\right\} \quad (34)$$

Where E_{T_0} is Young's modulus at room temperature, T_0 and e_{1-4} are the parameters of equation (34).

The measured 0.2% proof stress values for martensite and bainite were compared with those predicted using JMatPro®, and the results are reported in Figure 9.a). Considering the very good agreement obtained, JMatPro® predictions were used to estimate the 0.2% proof stress for temperatures for which experimental data were not available in the literature. Furthermore, given the importance of the mechanical properties of the austenitic phase during cooling for distortion prediction, the 0.2% proof stress of austenite was measured at different temperatures representing cooling during quenching, and fitted with the following equation [44]:

$$\sigma_{\mathrm{Y}}(T) = \sigma_{\mathrm{Y}_{T_0}}\left(r_5 + (1 - r_5)\exp\left\{-\frac{1}{2}\left(\frac{T - T_0}{r_3}\right)^{r_1} - \frac{1}{2}\left(\frac{T - T_0}{r_4}\right)^{r_2}\right\}\right) \quad (35)$$

Where $\sigma_{\mathrm{Y}_{T_0}}$ is the 0.2% proof is stress at room temperature and r_{1-5} are the parameters of equation (35).

The mechanical properties results as a function of temperature for different phases are shown in Figure 9.

In agreement with Mustak et al. [45], thermal expansion coefficient, α_k and structural dilatation due to volume change, Δ_k could also be calculated using the material density change, $\rho_k(T)$ of the phase k as a function of temperature, as reported in equations (36) and (37), respectively:

$$\alpha_k = \frac{1}{(T - T_0)} \times \left[\sqrt[3]{\frac{\rho_k(T)}{\rho_k(T_0)}} - 1\right] \quad (36)$$

$$\Delta_k = \frac{\Delta V_{a\to k}(T)}{V_a(T)} = \left[\frac{\rho_a(T) - \rho_k(T)}{\rho_a(T)}\right] \quad (37)$$

Where T_0 represents the room temperature and $V_a(T)$ the volume of austenite

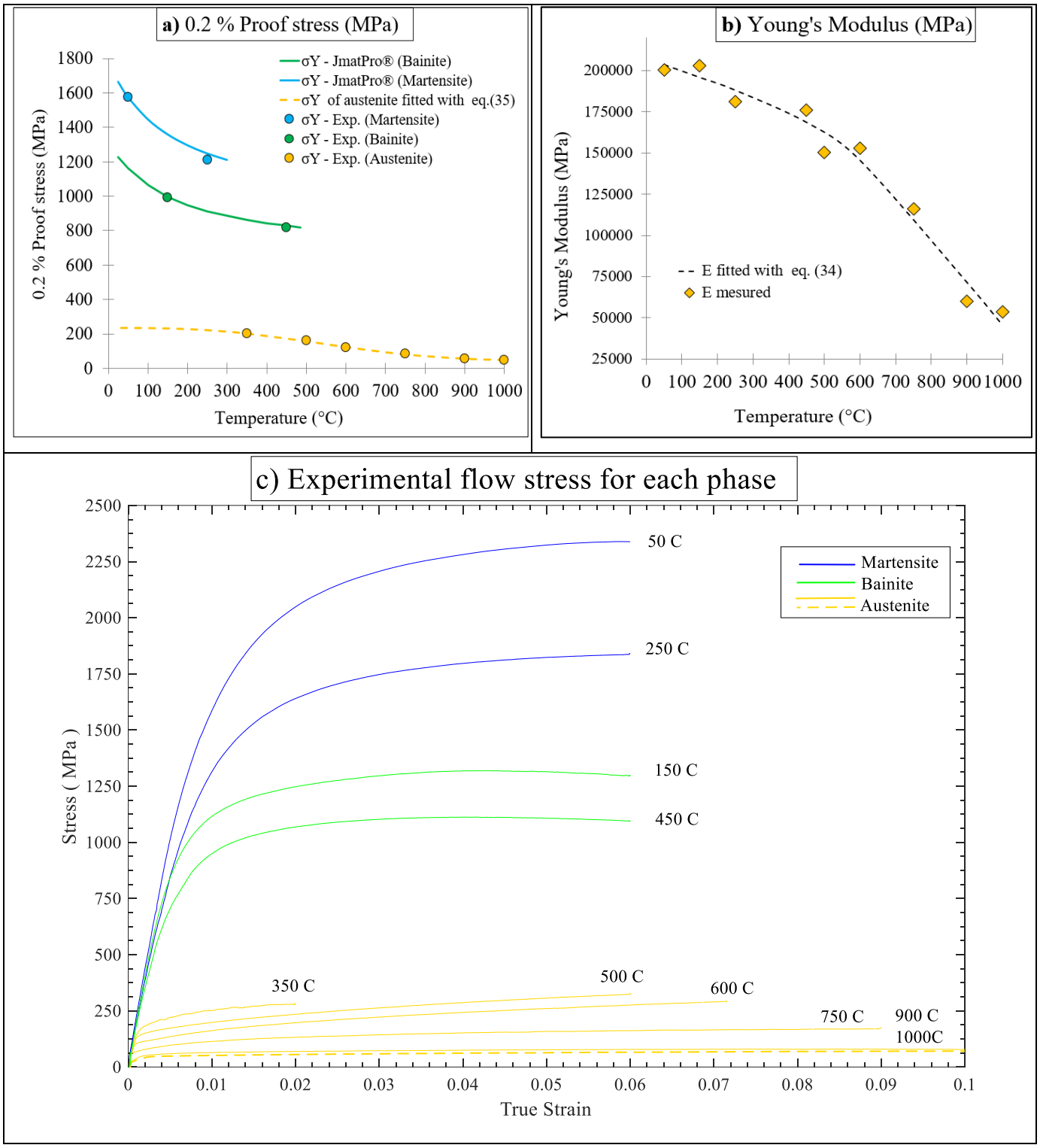

Figure 9: Experimental thermomechanical data as a function of temperature

The following equation uses the approximation of the Greenwood and Johnson [12] for the calculation of TRIP coefficient as a function of temperature, $K_k(T)$, including experimental data :

$$K_k(T) = \frac{5}{6}.\frac{\Delta V_{a\to k}(T)}{V_a(T)}.\frac{1}{\sigma_Y(T)} = \frac{5}{6}.\left(3.\varepsilon_k^{tp}(T)\right).\frac{1}{\sigma_Y(T)} \quad (38)$$

Where $\varepsilon_k^{tp}(T)$ represents the phase transformation strain (Figure 7) and $\sigma_Y(T)$ the 0.2% proof stress of austenite, as the softest phase (equation (35) - Figure 9.a))

3.3.1.2. TTT curves

Figure 10 illustrates the TTT (Temperature-Time-Transformation) diagram generated initially by JMatPro®, and then shifted down vertically to fit with the bainite transformation start temperature, Bs. The Bs and Ms temperatures were calculated using Kirkaldy and Haynes equations [31], respectively.

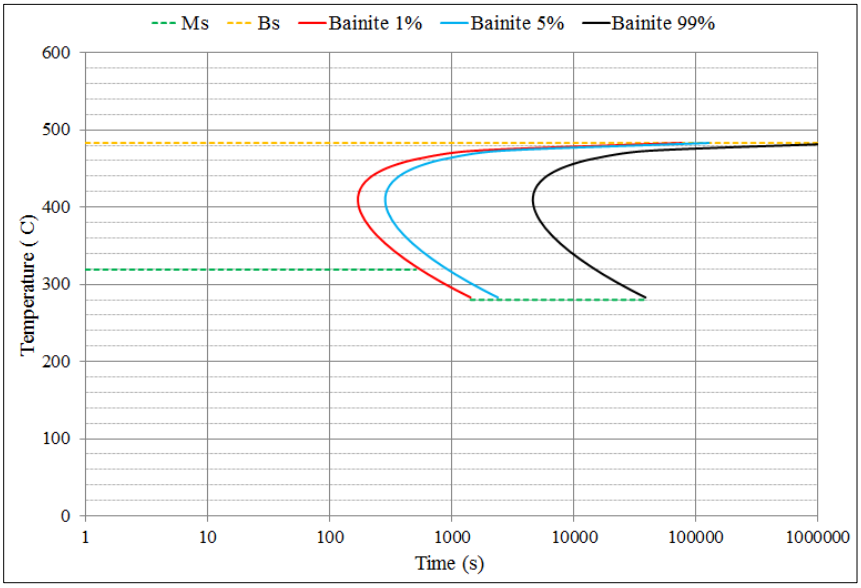

Figure 10: TTT generated initially by JMatPro® and modified to fit Bs

3.3.1.3. Thermo-physical data

The thermo-physical data such as the density, specific heat and thermal conductivity for each phase were generated by the JMatPro® software; the only exception was the thermal conductivity of the austenite, which was acquired from published experimental data on a steel that had a very close chemical composition to the one used in the present study [46]. Finally, the latent heat generation of bainite and martensite was calculated using the methods presented in [47] and [45], respectively.

4. Results and Discussion

4.1. Thermal analysis

Figure 11 shows the evolution of temperature during the quenching along y and z directions, starting from the center of the block, based on the FEM model predictions. A drastic temperature drop is observed due to the forced convection of water over the block, which results in a flat-top Gaussian temperature distribution (Figure 11.a). On the other hand, this effect is countered by the high thermal inertia (high Biot number) of the block, through conduction, which results in maintaining high temperature at the center, even after 900s. As the size of the colder regions increases, the maximum temperature at the center decreases progressively to form a Gaussian shape temperature distribution pattern.

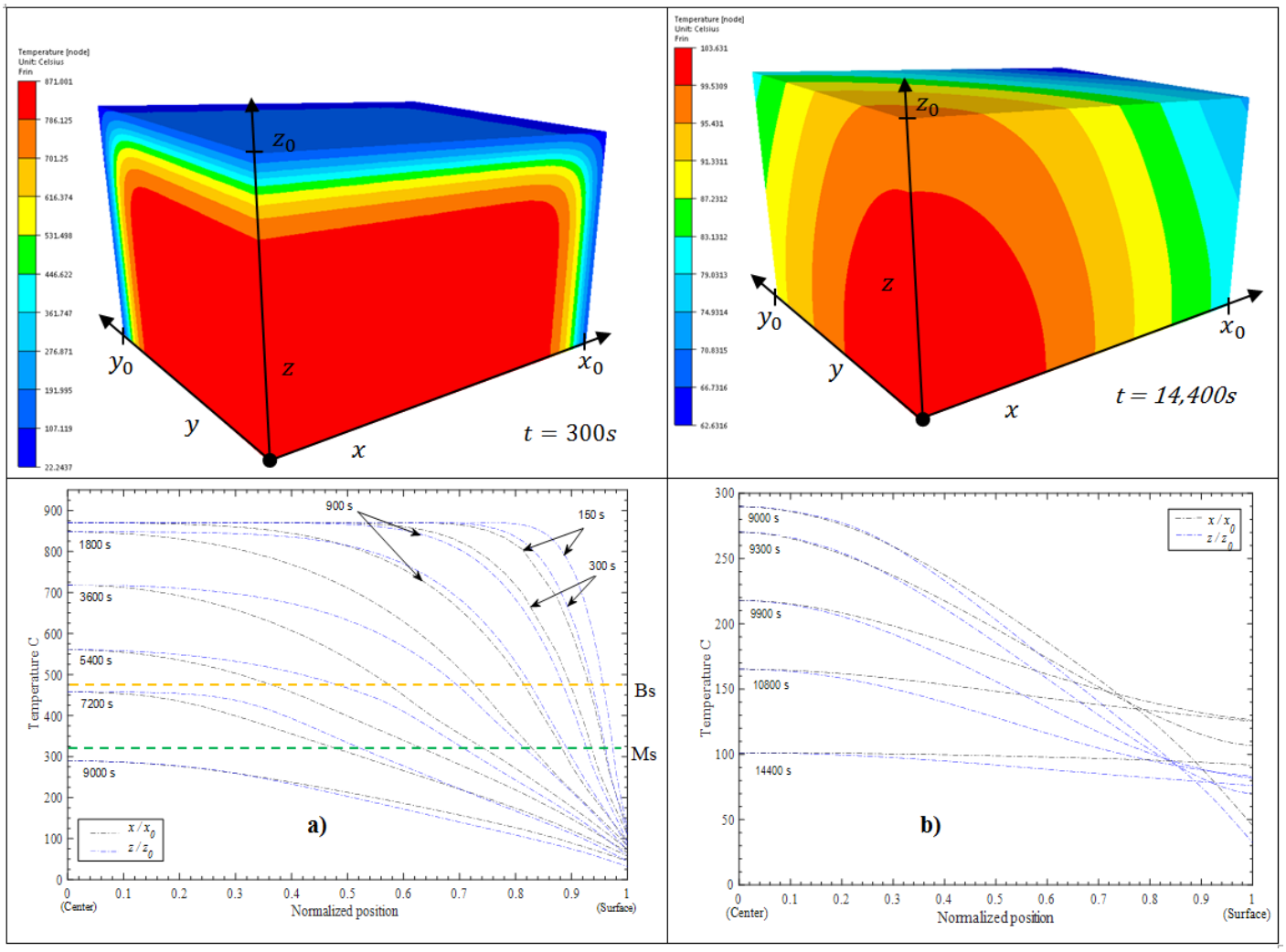

Figure 11: Evolution of temperature along *x* and *z* directions during **a)** water quenching, and **b)** air cooling

As illustrated in section 3.1, the block was taken out from the quench water bath after 2.5h to be cooled in the air. All phase transformations (e.g., austenite to martensite, austenite to bainite) were expected to reach the finishing stage for the full block (temperature below M_S). From Figure 11.b), it can be concluded that the heat stored in the center region of the block was transferred to the surfaces by conduction, due to the low severity of air cooling (low HTC), based on the fact that the temperature difference inside the block quickly vanished between the center and surfaces. Based on the above analysis, it can be said that the calculated temperature for the block was accurately predicted considering the similarity of the quench conditions (steel grade, thickness of the block, size of the quench tank, etc.) to experimental works published by some of the current authors [27].

4.2. Distortion analysis:

Figure 12 illustrates the prediction of shape change during quench, where it can be seen that the maximum displacements are mainly located at the center of the surfaces. However, the level of distortion was pronounced for the surfaces normal to the z direction, with a maximum value of 7.6 mm at the surface center. The external shape of the block, scanned after quenching (Figure 14), confirmed a characteristic shape that is usually observed in the case of steel hardening of a prismatic specimen [12]. The geometry obtained after hardening could be described mainly by a spool shape characterized by a bulging out at the edges and a bulging in at the center of the surfaces, as also reported by J.H. M. Schwenk, et al. (2014) [12].

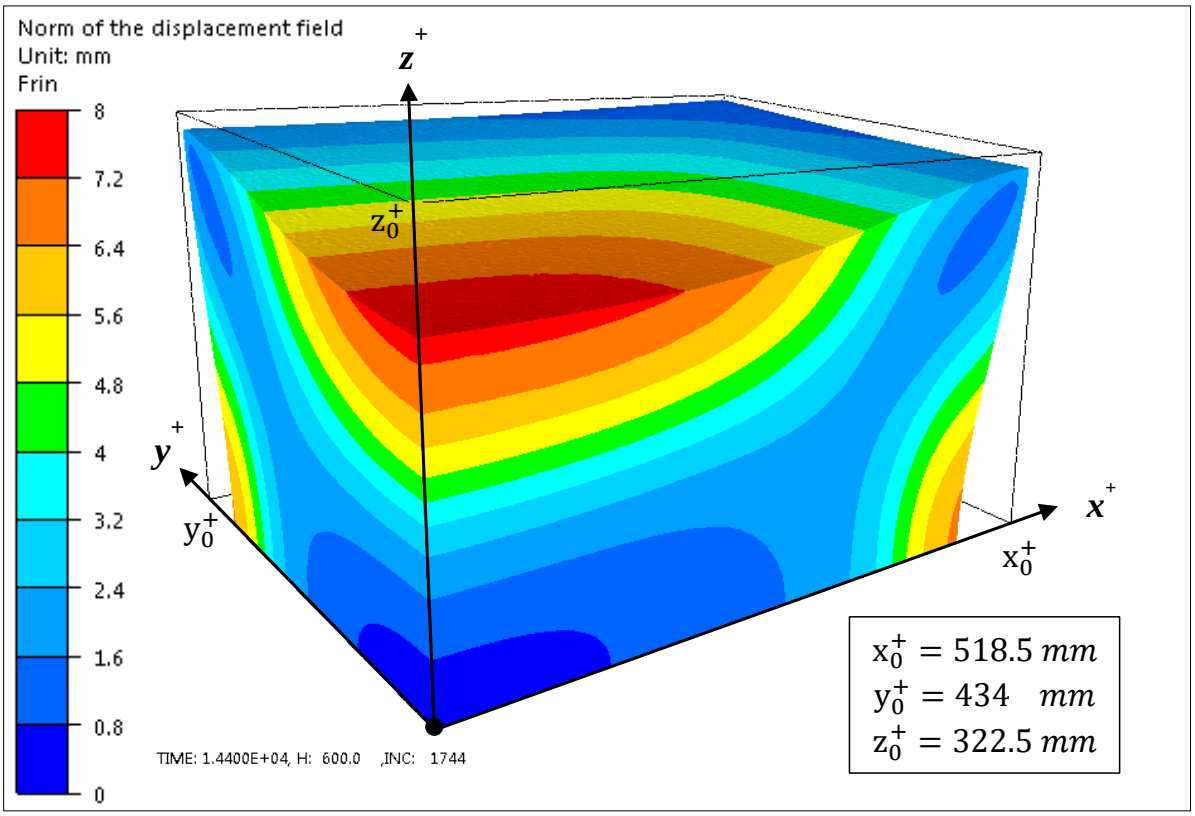

Figure 12: Distortion pattern obtained after quench simulation (× 10 displacement magnification)

4.2.1. Distortion evolution during quench

The progress of the predicted distortions via a temporal sequence of cross-sectional volume changes at $(x_0\, z_0)$ was tracked using the same magnitude (×10) and level of iso-displacement (black lines) superimposed with temperature, as illustrated in Figure 13. The simulation of the early stages of water quenching (Figure 13, t = 150s, 300s) shows that the iso-displacements are mainly located at the surface, and have a convex shape (maximum displacement in z^+ direction, was located next to the bulging edges). At this stage, a good correlation between the temperature and displacement fields could be observed, indicating that the shrinking of the block was driven by thermal stresses. T. Lübben, et al. (2014) reported that the temperature difference $\Delta T = (T_{max} - T_{min})$ between the coldest and hottest zones could be correlated to the intensity of thermal stresses [48, 49]. Results reported in Figure 13 also reveal that due to high heat removal, the edges were the first elements to experience Ms temperature [19, 23] and build a rigid frame composed of hard martensitic

layers. This newly formed martensite (fresh martensite) is associated with a fast increased volume change that could explain the local bulging out of the iso-displacement at the level of the edges while the iso-displacements of the untransformed zones within the block still keep a convex shape (Figure 13, t = 150s, 300s). The observed geometry could be mostly described by a barrel-shape; the martensitic transformation starts first in the surface regions before ΔT is at a maximum, and the remaining zones being still in the austenitic state at high temperature [4]. Results indicate that at around t = 900s, $\Delta T \approx \Delta T_{max}$, the maximum level of thermal stresses has probably been reached and that the deviation between the temperature and displacement fields can be clearly observed. In the time interval 900s-to-9000s, the magnitude and extent of transformational stresses increase as the phase transformation continues to spread progressively towards the center of the block. The shape changes at this stage are mostly controlled by the transformational stresses that overcome thermal stresses (continuous decrease of ΔT), resulting in progressive shape evolution from a barrel to a spool shape [13, 48] . In other words, z_{min} in (x_0,z_0), the cross-section is moving from the edge region to the center at the level of the top surface. During air quenching, phase transformations are expected to be in their finishing stage (temperatures below *Ms*), and therefore, volume changes are slightly noticeable, with a rapid decrease of ΔT (Figure 13, t = 9000s to 14,400s). Therefore, it could be said that as long as the temperature is below any critical phase transformation value (e.g., M_f) and ΔT is very small, the block has almost attained its final shape.

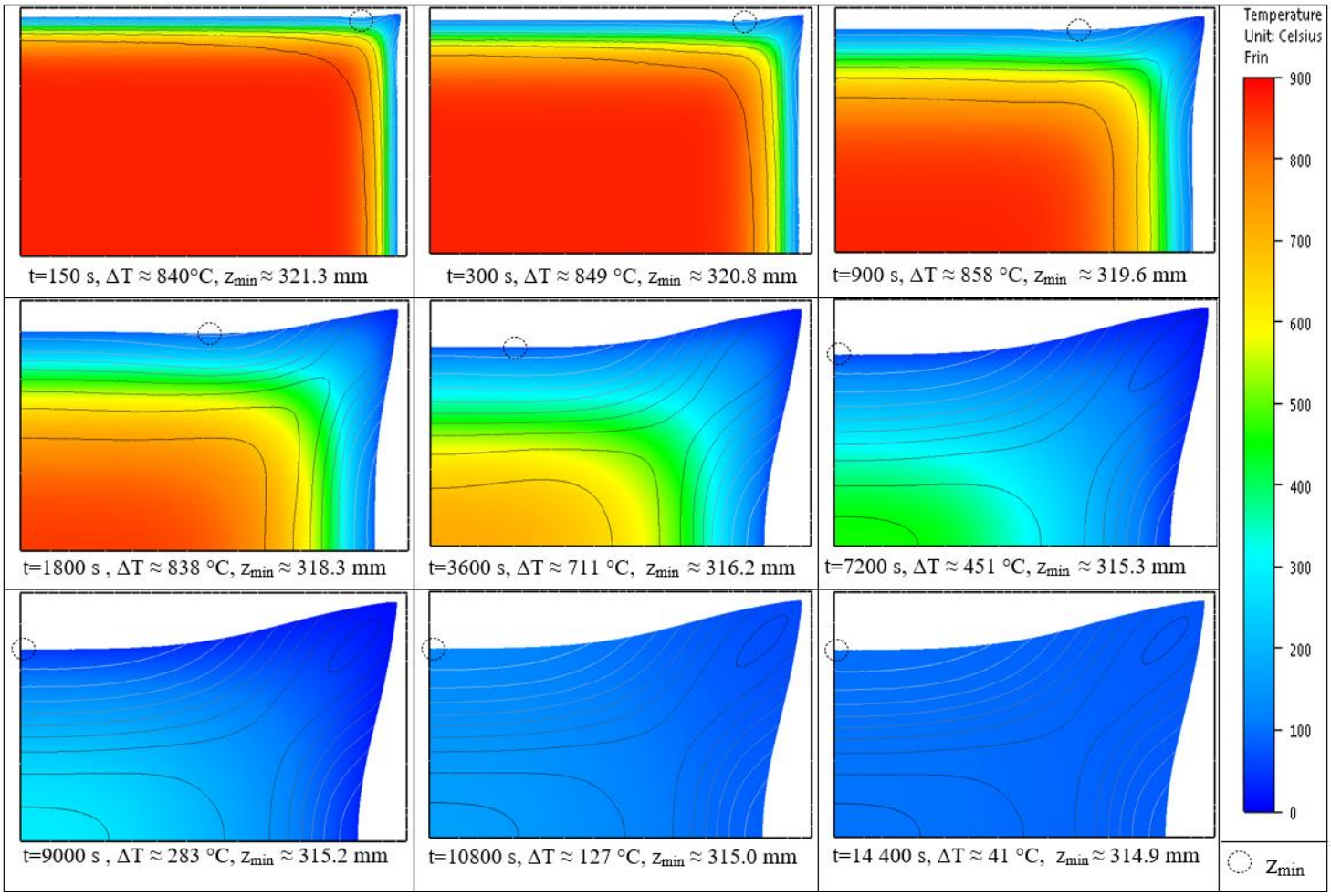

Figure 13: Evolution of (x_0, z_0) cross-section volume change superimposed with temperature evolution

4.2.2. Experimental validation of predicted distortions

The reconstructed shape after the heat treatment was used for the evaluation of thickness changes. As shown in Figure 14.b), a coordinate grid (14×12) was extracted from the upper ($z_+(x,y)$) and bottom ($z_-(x,y)$) surfaces to be analyzed in MATLAB in order to model thickness change, $z_{thickness} = (z_+ - z_-)$ along x-y plane. The results obtained, reported in Figure 14.a, show that the maximum thickness change reaches almost 630 mm in the center of the block, corresponding to a thickness reduction of about 15.2 mm, as compared to the nominal thickness, $z_0=645$ *mm*. However, the apex was not positioned exactly at the center of the block (as predicted by simulation results shown in Figure 12), but rather, was shifted by 100 mm in the y_0-

direction, and tilted about 5.3°. The positioning deviation observed between experimental measurements and the simulation results could be explained by the imperfection of the initial shape, which was considered perfectly prismatic, as well as the homogenous heat transfer at all faces for the simulation purposes.

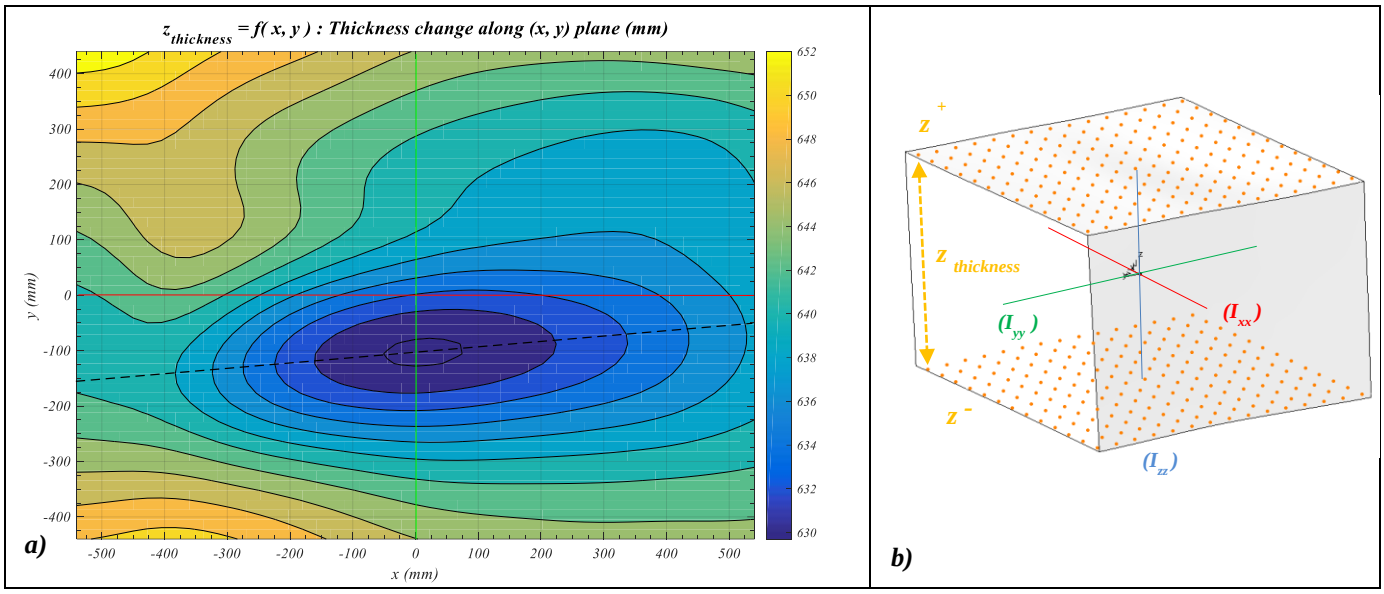

Figure 14: ***a)*** Thickness change ($z_{thickness}$) after hardening as a function of *(x,y)* coordinates, ***b)*** Data extraction procedures from the reconstructed block

Figure 15 shows a comparison between the thickness reduction **($\Delta z = z_{thickness} - z_0$)** calculated by the FEM model at ***y = 0*** and the measured one at the indicated cross-section in Figure 14 (black dashed line). It is important to mention that the simulation was forced to continue for air cooling after 14,400s to vanish the existing ΔT as much as possible, from *41°C to 7.5°C* (after 45,000s). This was done with the aim of analyzing the final shape state with a uniform temperature. The thickness deviation predicted by simulation using experimental data followed a trend similar to the experimental observations. The maximum thickness reduction was accurately predicted versus the measured one, with a deviation of about 0.5 mm. As mentioned above, the measured distortion was not perfectly symmetrical, which explains the slight difference in the results on the right part of the block. It must also be emphasized that considering the large size of the block, particularly its thickness, it is reasonable to assume that some microstructural heterogeneity

(e.g., macro-segregation, grain size variation, etc.) may exist within the block, and as such, the block may not be symmetrical as well, which may influence the distortion level for each face.

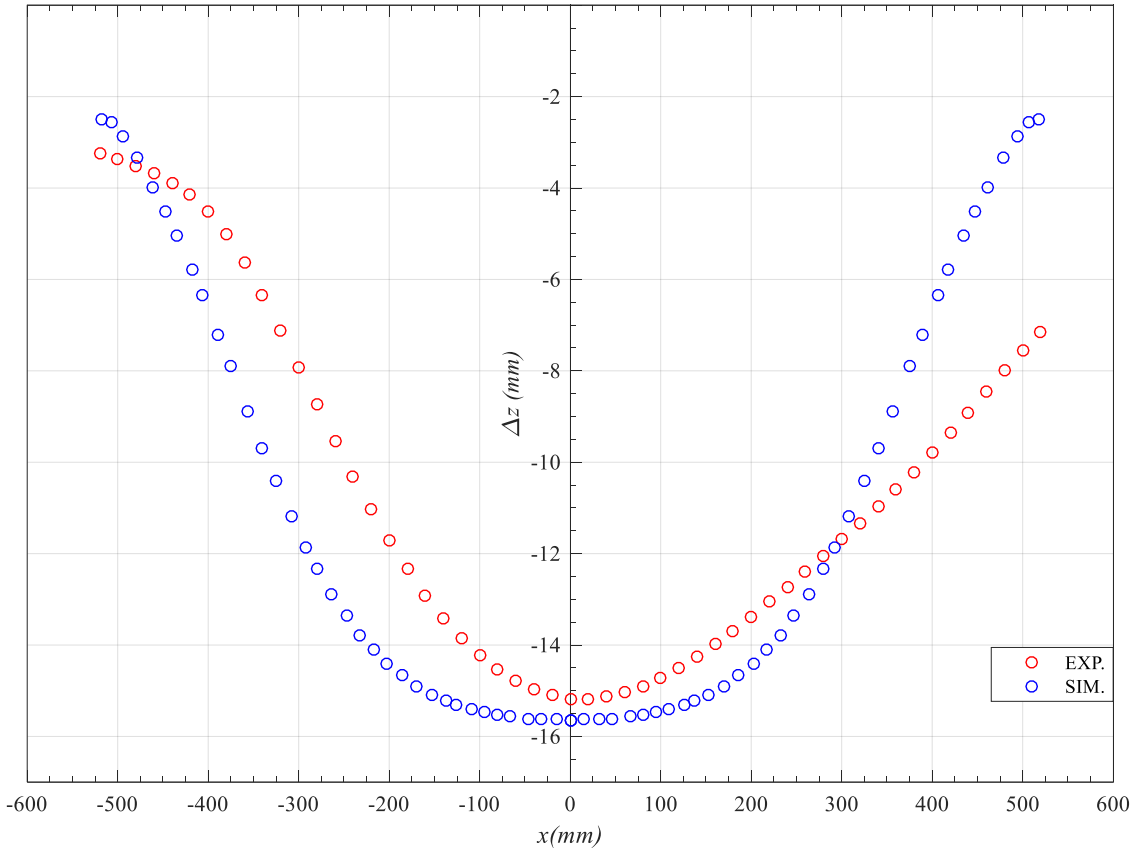

Figure 15: Thickness reduction, Δz: Comparison between the measured and the simulated values.

4.3. Residual stresses

The final state of Von Mises residual stresses calculated after quench could be directly linked to the superposition of thermal and transformational effects. Figure 16 shows that the most critical residual stresses are generally located in the center region of surfaces, with the maximum magnitude of residual stress at the level of the smaller surfaces. This could be explained by the fact that the smaller surfaces are cooled faster than the larger ones (as reported in Figure 11.a), which results in higher thermal stresses and an increase in the Von Mises stress for the smaller surfaces. In the same figure, it can be seen that the surface in the

thickness direction experienced the maximum deformation, as compared to other surfaces. This higher plastic deformation is probably what mainly accounts for the magnitude of the reduction of residual stresses observed on these surfaces [48].

The maximum level of residual stress was reached at around 1794 MPa, which exceeds the martensite yield stress at room temperatures (1650 MPa), thus indicating the possibility of cracking. The stress-strain curve of martensite at room temperature shown in Figure8.c) demonstrates that the martensite phase is able to resist stresses up to 2350 MPa, which could mean that the stresses experienced at the surface, even when they exceed the yield stress of martensite, could be absorbed via plastic deformations. Furthermore, at the surface level, the principal stress components, S_{33} and S_{22}, show negative values at the center, while S_{11} was positive and localized near the edges. Thus, the distribution of the Von Mises residual stress and that of the principal stress, S_{33}, could be correlated, indicating that the external layers at the surface level experienced high compressive stresses, while the rest of the block was under low tensile stresses to balance this effect [19]. The formation of the compressive stresses near the surface regions are considered beneficial as they increase the service life of the forgings [48].

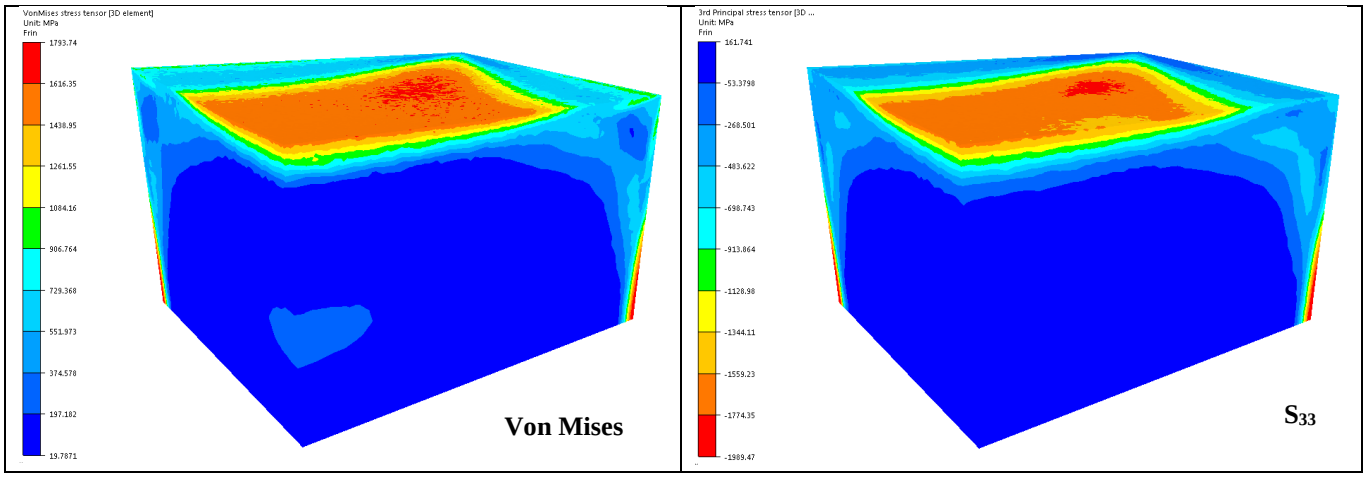

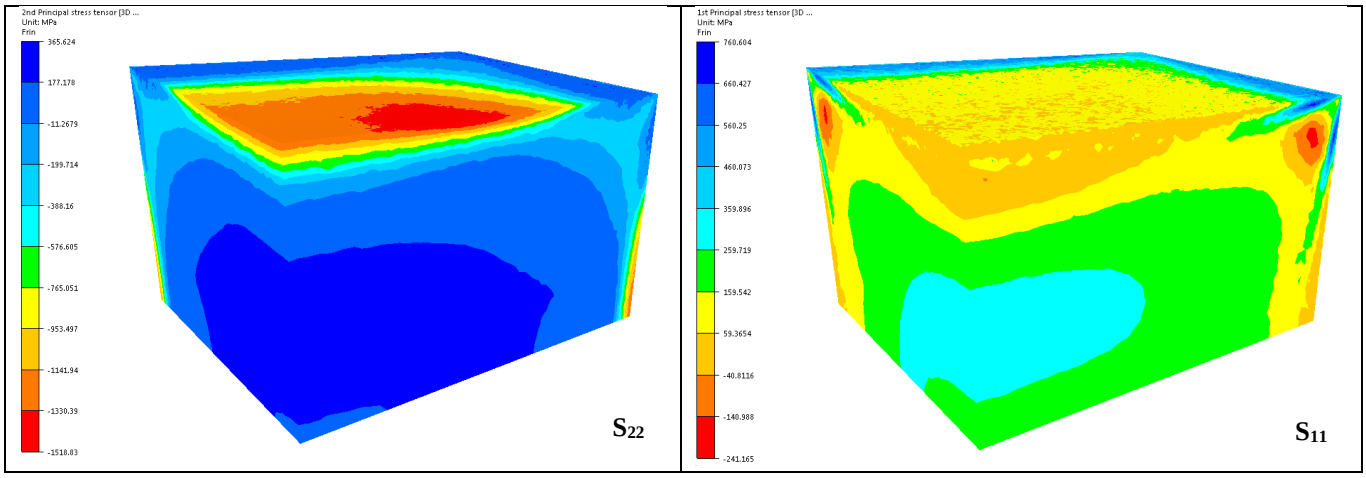

Figure 16: Distribution of residual stresses at the end of the quench process

5. Conclusions

FEM modeling supported by experimental validation was used to investigate the distortion and residual stress distribution during water quenching of a large size forged steel block. It should be mentioned that to the best knowledge of authors, it is the first time in the literature, that the distortion measurements were made tri-dimensionally for such large size heat treated steel blocks.

The following conclusions can be drawn from the present study:

1. A methodology was proposed for reliable measurement of quench induced distortions of large size forged blocks and a good agreement was obtained with FEM predictions.
2. The distortion is mainly driven by the volume expansion coefficient, the volume change due to phase transformation and the TRIP effect. These quantities significantly influence the estimation of strains and displacements.
3. The quality of experimental data coming from dilatometry tests plays an essential role in the accurate distortion prediction by the FEM model.
4. The distortion trend as well as the maximum thickness reduction at the center of the block was predicted with enough precision for industrial application.

Considering that the experimental validation of the predicted residual stresses was not possible due to the large size of the block (danger: possibility of crack during measurement operations), the estimated values for residual stresses could be considered reasonable due to the accuracy of flow stress determination for each phase.

Further research needs to look at the heterogeneity of the cooling rate experienced by each face and further, to consider the material's orthotropic character and its impact on simulations.

Acknowledgement

This project was realized in collaboration with Finkl Steel-Sorel. A portion of the grant used for this collaboration was supported by MITACS (IT03151), which is gratefully acknowledged. The authors are also very grateful to Finkl Steel, especially the R&D and Engineering departments, for providing the large size block, as well as the instrumentation and measurements used in the present research.

References

[1] A. Michael, K. Nikolai, P. Joseph, Industrial-scale intensive quenching process for tool products commercialization, in: EMTEC report no. EMTEC CT-76-II, Edison Material Technology Center (EMTEC), Dayton, OH, USA, 2005.
[2] H.-W. Yen, M.-H. Chiang, Y.C. Lin, D. Chen, C.-Y. Huang, H.-C. Lin, High-Temperature Tempered Martensite Embrittlement in Quenched-and-Tempered Offshore Steels, Metals, 7 (2017) 253.
[3] L. He, L. Huiping, FEM simulation of quenching residual stress for the plane strain problems, 2010 International Conference on Computer Design and Applications, ICCDA 2010, 3 (2010).
[4] M. Narazaki, G. Totten, G. Webster, Hardening by reheating and quenching, ASM International, Member/Customer Service Center, Materials Park, OH 44073-0002, USA, 2002., (2002) 248-295.
[5] D. Koen, S. Marc, The Effect of Size on the Distortion Behavior After Carburisation and Quenching Processes of Gears, Int J Metall Mater Eng 3(2017).
[6] W.P. de Oliveira, M.A. Savi, P.M.C.L. Pacheco, Finite element method applied to the quenching of steel cylinders using a multi-phase constitutive model, Archive of Applied Mechanics, 83 (2013) 1013-1037.
[7] D. Huang, K. Arimoto, K. Lee, D. Lambert, M. Narazaki, Prediction of Quench Distortion on Steel Shaft with Keyway by Computer Simulation, ASM Proceedings: Heat Treating, 2 (2000) 708-712.
[8] A. Thuvander, Numerical simulation of gas quenching of tool steels and the influence of hardenability on distortion, in: 6th International Tooling Conference, Karlstad, Sweden, 2002, pp. 625-642.
[9] C. Simsir, Transformation Induced Plasticity (TRIP) of SAE 52100 Steel during Martensitic and Bainitic Transformations, Hittite Journal of Science & Engineering, 4 (2017).
[10] Y. Vincent, J.-F. Jullien, P. Gilles, Thermo-mechanical consequences of phase transformations in the heat-affected zone using a cyclic uniaxial test, International Journal of Solids and Structures, 42 (2005) 4077-4098.
[11] J.-y. Liu, H. Lu, C. Junmei, Experimental analysis of transformation induced plasticity in 9Cr1Mo steel, Frontiers of Materials Science in China, 3 (2009) 61-66.
[12] J.H. M. Schwenk, and V. Schulze, Karlsruhe Institute of Technology, Residual Stresses and Distortion in Quenched and Tempered Steels, in: J. Dossett and G.E. Totten (Ed.) ASM Handbook, Volume 4B, Steel Heat Treating Technologies, ASM International, 2014.
[13] C. Şimşir, Modeling and Simulation of Steel Heat Treatment—Prediction of Microstructure, Distortion, Residual Stresses, and Cracking, ASM Handbook, 4 (2014) 409-466.
[14] L. Cheng, Z. Liwen, Q.a. Zhang, Z. Quying, W. Zhaokun, Numerical Simulation and Technological Parameter Optimization for Quenching Process of a Gas Turbine Compressor Disk Based on Metallo-Thermo-Mechanics, J. Mater. Sci. Technol., 22 (2006) 860-864.

[15] K. Perzynski, L. Madej, A. Szajding, K. Raga, K. Kubiak, A. Niechajowicz, K. Jaskiewicz, Z. Gronostajski, M. Pietrzyk, Numerical evaluation of gear ring behavior during various cooling conditions, Journal of Machine Engineering, 16 (2016) 18-26.
[16] H. Li, G. Zhao, L. He, Y. Mu, High-speed data acquisition of the cooling curves and evaluation of heat transfer coefficient in quenching process, Measurement, 41 (2008) 676-686.
[17] I. Felde, S. Szénási, A. Kenéz, S. Wei, R. Colas, Determination of complex thermal boundary conditions using a Particle Swarm Optimization method.
[18] H.S. Hasan, M.J. Peet, J.M. Jalil, H.K.D.H. Bhadeshia, Heat transfer coefficients during quenching of steels, Heat Mass Transfer, 47 (2011) 315-321.
[19] S.H. Kang, Y.T. Im, Thermo-elasto-plastic finite element analysis of quenching process of carbon steel, Journal of Materials Processing Technology, 192–193 (2007) 381-390.
[20] S.-H. Kang, Y.-T. Im, Three-dimensional thermo-elastic–plastic finite element modeling of quenching process of plain-carbon steel in couple with phase transformation, International Journal of Mechanical Sciences, 49 (2007) 423-439.
[21] G.E. Evcil, O. Mustak, C. Şimşir, Simulation of through-hardening of SAE 52100 steel bearings – Part II: Validation at industrial scale, Materialwissenschaft und Werkstofftechnik, 47 (2016) 746-754.
[22] M. Boniardi, M. Guagliano, A. Casaroli, R. Andreotti, F. Ballerini, Large Forgings: Microstructural Evolution and Residual Stresses Due to Quenching Treatments—A Combined Numerical and Experimental Approach, (2014).
[23] G.Y. Liu, L.M. Dong, K.K. Wang, D.M. Zhu, S.J. Zhang, S.C. Gong, M.W. Li, Water–air online quenching process of 3Cr2Mo steel based on numerical simulation, Ironmaking & Steelmaking, 43 (2016) 780-789.
[24] FORGE®NxT, http://www.transvalor.com/en/cmspages/traitement-thermique.62.html, in.
[25] C. Şimşir, Simulation of Quenching, Handbook of Thermal Process Modeling of Steels, in, CRC Press-Taylor & Francis Group, 2009.
[26] B. Liščić, Steel Heat Treatment, in: Steel Heat Treatment, CRC Press, 2006.
[27] Y. Bouissa, D. Shahriari, H. Champliaud, M. Jahazi, Prediction of heat transfer coefficient during quenching of large size forged blocks using modeling and experimental validation, Case Studies in Thermal Engineering, 13 (2019) 100379.
[28] Dung-An Wang, Computational Modeling of a Jominy Test Proceedings of the 29th National Conference on Mechanical Engineering of CSME, December 6-7, 2013, I-Lan, Taiwan, (2013).
[29] J.G. Dong-li Song , Jiansheng Pan , Xin Yao, Design of Quenching Process for Large-sized AISI P20 Steel Block Used as Plastic Die, Journal of Materials Science & Technology, (2006).
[30] C. Aliaga, Simulation numérique par élément finis en 3D du comportement thermomécanique au cours du traitement thermique d'aciers : Application a la trempe de pieces forgées ou coulées, in, Ecole Nationale Supérieure des Mines de Paris, 2000.
[31] D. Cardinaux, Étude et modélisation numérique 3D par éléments finis d'un procédé de traitement thermique de tôles embouties après chauffage par induction : application a un renfort de pied central automobile, in: Ecole Doctorale 364 : Sciences Fondamentales et Appliquées, Ecole Nationale Supérieure des Mines de Paris, 2008.
[32] N. Saunders, U.K.Z. Guo, X. Li, A.P. Miodownik, J.P. Schillé, Using JMatPro to model materials properties and behavior, JOM, 55 (2003) 60-65.
[33] G. Guzzetta, Relating Deformation and Thermodynamics: An Opportunity for Rethinking Basic Concepts of Continuum Mechanics, Entropy, Entropy (2013) 2548-2569.
[34] D. Tong, J. Gu, F. Yang, Numerical simulation on induction heat treatment process of a shaft part: Involving induction hardening and tempering, Journal of Materials Processing Technology, 262 (2018) 277-289.
[35] C. Şimşir, A Mathematical Framework for Simulation of Thermal Processing of Materials: Application to Steel Quenching, Turkish Journal of Engineering and Environmental Sciences, (2008) 85–100.
[36] C. Şimşir, 3D Finite Element Simulation Of Steel Quenching In Order To Determine The Microstructure And Residual Stresses, in: The Graduate School Of Natural And Applied Sciences, Middle East Technical University, 2008.
[37] D. Tong, J. Gu, G.E. Totten, Numerical investigation of asynchronous dual-frequency induction hardening of spur gear, International Journal of Mechanical Sciences, 142-143 (2018) 1-9.
[38] H. Li, G. Zhao, L. He, Finite element method based simulation of stress–strain field in the quenching process, Materials Science and Engineering: A, 478 (2008) 276-290.
[39] B.R. Barbero, E.S. Ureta, Comparative study of different digitization techniques and their accuracy, Computer-Aided Design, 43 (2011) 188-206.
[40] T. Tóth, J. Živčák, A Comparison of the Outputs of 3D Scanners, Procedia Engineering, 69 (2014) 393-401.
[41] J. Peraire, S. Widnall, Lecture L26 - 3D Rigid Body Dynamics: The Inertia Tensor, in: M. OpenCourseWare (Ed.) Dynamics, 2008.
[42] B.K. Choudhary, E.I. Samuel, K. Bhanu Sankara Rao, S.L. Mannan, Tensile stress–strain and work hardening behaviour of 316LN austenitic stainless steel, Materials Science and Technology, 17 (2001) 223-231.
[43] Z.X. Li, M. Zhan, X.G. Fan, J.Q. Tan, A modified Johnson-Cook model of as-quenched AA2219 considering negative to positive strain rate sensitivities over a wide temperature range, Procedia Engineering, 207 (2017) 155-160.

[44] M. Seif, L. Choe, J. Gross, W. Luecke, J. Main, D. McColskey, F. Sadek, M. Seif, J. Weigand, C. Zhang, Temperature-dependent material modeling for structural steels: formulation and application, US Department of Commerce, National Institute of Standards and Technology, 2016.
[45] O. Mustak, E. Evcil, C. Şimşir, Simulation of through-hardening of SAE 52100 steel bearings – Part I: Determination of material properties, Materialwissenschaft und Werkstofftechnik, 47 (2016) 735-745.
[46] J. Cochet, S. Thuillier, T. Loulou, N. Decultot, P. Carré, P.-Y. Manach, Heat treatment of 34CrNiMo6 steel used for mooring shackles, The International Journal of Advanced Manufacturing Technology, 91 (2017) 2329-2346.
[47] A. Kulawik, A. Bokota, Modelling of Heat Treatment of Steel Elements with the Movement of Coolant, 56 (2011) 345.
[48] T. Lübben, J. Dossett, G. Totten, Basics of distortion and stress generation during heat treatment, ASM Handbook, 4 (2014) 339-354.
[49] N.I. Kobasko, W.S. Morhuniuk, B.K. Ushakov, Design of Steel-Intensive Quench Processes, CRC Press, New York, 2007.